Supplementary Information of

Valorization of Sargassum spp. for bio-inspired synthesis of ZnO/Au nanocomposites used in SERS detection of trace herbicides

MATERIALS AND METHODS

Preparation and standardization of Sargassum extract

The DPPH assay measures the capacity of an antioxidant to reduce the stable free radical DPPH. First, a 50 µM DPPH solution was prepared in a 40:60 v/v buffer containing 0.1 M acetic acid in ethanol and methanol. Next, 150 µL of the extract and 2850 µL of the prepared DPPH solution were mixed and kept in the dark for 30 min to allow the reaction between the DPPH radical and the hydrogen donors present in the extract. After this lapse, the absorbance of the mixture was measured at 517 nm using a UV–Vis spectrophotometer. Trolox (dissolved in ethanol) was used as a standard, and results were expressed in micromoles of Trolox equivalents per gram of dry extract (µmol Teq/g). All experiments were performed using a 1 cm^2 quartz cuvette.

The CUPRAC assay works by converting copper (II) ions (Cu II) into a copper (I) neocuproine complex (Cu I-Neocuproine) through a reaction with antioxidants. First, the CUPRAC reagent was prepared by mixing 1 mL of 10 mM copper (II) chloride aqueous solution, 1 mL of 7.5 mM neocuproine ethanolic solution, and 1 mL of 1 M ammonium acetate buffer (pH 7) aqueous solution. Then, 100 µL of the extract was mixed with the CUPRAC reagent and incubated in the dark for one hour. Finally, the absorbance at 450 nm was measured with a UV-Vis spectrophotometer, using Trolox (dissolved in ethanol) as the standard. Results were reported as micromoles of Trolox equivalents per gram of dry extract (µmol Teq/g). All experiments were performed using a 1 cm^2 quartz cuvette.

The compounds in the extract, such as phenols and flavonoids, were also quantified by UV–Vis spectroscopy. All experiments were performed using a 1 cm^2 quartz cuvette. For TPC determination, the Folin-Ciocalteu reagent was utilized. The assay consists of mixing 1 mL of the extract with 5 mL of a 10% v/v Folin-Ciocalteu aqueous solution and 4 mL of a 7.5% w/v sodium carbonate aqueous solution. The mixture was incubated in the dark for 1 hour, and the absorbance was measured at 765 nm using a UV-Vis spectrophotometer. In this case, gallic

acid was used as the reference compound. The results were expressed as micromoles of gallic acid equivalent per gram of dry extract (µmol GAeq/g).

For the FC assay, first, 1 mL of the extract was mixed with 100 µL of 2% w/v aluminum chloride ($AlCl_3$) solution (prepared with a 5% w/v acetic acid-methanol buffer (AAB)), and next was diluted to 2.5 mL with the AAB. The solution was kept in the dark for 30 min before measuring absorbance at 415 nm using UV-Vis spectroscopy. Morin, a flavonoid, was used as the standard. Results are reported as micromoles of morin equivalent per gram of dry extract (µmol Meq/g).

The standardization results are summarized in Table S1 for the water extraction and in Table S2 for the water/ethanol extraction. Gravimetric yield, TAC, TPC, and FC data are presented for each extraction replicate, along with the average, standard deviation (SD), standard error (SE), and relative standard deviation (RSD). It is important to note that the extraction parameters (temperature, agitation, sargassum immersion time, and m/v ratio) must be carefully controlled to ensure reproducibility, as these values can vary significantly if the process is not standardized. Therefore, it is recommended to characterize the extract prior to synthesis to achieve better control of the variables.

Table S1. Results of *sargassum* water extract standardization

Extraction replicate	***Yield (%)***	***TAC***		***TPC (µmol GAeq/g).***	***FC (µmol Meq/g)***	***FC/TPC ratio***
		DPPH (µmol Teq/g)	***CUPRAC (µmol Teq/g)***			
Ext-1	*21.30*	*35.75*	*58.41*	*30.92*	*11.00*	*0.36*
Ext-2	*18.60*	*33.95*	*51.59*	*27.30*	*9.20*	*0.34*
Ext-3	*20.30*	*35.91*	*59.10*	*28.30*	*9.81*	*0.35*
Average	*20.08*	*35.20*	*56.37*	*28.84*	*10.00*	*0.35*
SD	*±1.37*	*±1.09*	*±4.15*	*±1.87*	*±0.91*	*±0.01*
SE	*±0.79*	*±0.63*	*±2.40*	*±1.08*	*±0.53*	$\pm 5.4*10^{-3}$
RSD (%)	*6.81*	*3.09*	*7.36*	*6.48*	*9.15*	*2.71*

Table S2. Standardization results of 1:1 (v/v) water/ethanol *sargassum* extract

Extraction replicate	***Yield (%)***	***TAC***		***TPC (µmol GAeq/g).***	***FC (µmol Meq/g)***	***FC/TPC ratio***
		DPPH (µmol Teq/g)	***CUPRAC (µmol Teq/g)***			
Ext-1	*4.33*	*192.29*	*403.92*	*102.90*	*26.00*	*0.35*
Ext-2	*4.20*	*214.33*	*477.57*	*117.03*	*37.9*	*0.32*
Ext-3	*4.83*	*176.01*	*408.81*	*106.14*	*41.9*	*0.39*
Average	*4.46*	*194.21*	*430.10*	*108.69*	*38.6*	*0.35*
SD	*±0.33*	*±19.23*	*±41.18*	*±7.40*	*±3.01*	*±0.036*
SE	*±0.19*	*±11.10*	*±23.78*	*±4.27*	*±1.73*	*±0.021*
RSD (%)	*7.49*	*9.90*	*9.57*	*6.81*	*7.80*	*10.07*

SERS substrates preparation

Glass microscope slides served as the base surface for ZnO/Au NP deposition. They were first thoroughly cleaned by immersion in a 70% ethanol/water solution in a Coplin jar for 2 minutes, then rinsed with distilled water and stored temporarily in water until use. All prepared substrates were stored in a dust-free environment until required for SERS measurements. For the stock solutions of glyphosate and ammonium glufosinate, an initial concentration of 25 mM was prepared in distilled water. A stock solution of potassium iodide (KI) was prepared at 0.1 M in distilled water. All stock solutions were stored in amber glass bottles protected from light. Working solutions for SERS analysis were prepared by mixing the herbicide stock solution and the KI solution in a 1:1 volume ratio. Serial dilutions were performed to achieve final herbicide concentrations: 30 µM, 20 µM, 15 µM, 10 µM, 1 µM, 50 nM, 50 pM, 50 fM, 50 aM, 50 zM, and 50 yM. Both the initial stock solutions and all subsequent working dilutions were prepared in triplicate.

ZnO/AuNPs SERS substrates were prepared starting from a ground catalyst material (ZnO/Au-1, ZnO/Au-2, or ZnO/Au-5 NPs). Dispersions were prepared by weighing 1 mg of the catalyst, adding 40 µL of isopropanol, and sonication for 15 minutes. Subsequently, 10 µL of Nafion™ 117 was added as a binding agent, followed by an additional 10 minutes of sonication. To create the colloidal film, 3 µL of the final ZnO/AuNPs dispersion was drop-cast onto a clean glass slide and allowed to air-dry. This process was repeated to apply three additional layers.

A final aliquot of 9 µL of the dispersion was added, resulting in a circular film with a diameter of approximately 3 mm ± 0.05 mm (area ≈ 0.0707 cm^2). To improve NPs' adhesion to the glass surface, the prepared slides were heat-treated in an oven at 70 °C overnight. For comparative purposes, reference substrates using only ZnO nanoparticles (NPs) were prepared following the same procedure.

Spectroscopic analysis and SERS sensor performance

Raman and SERS spectra were acquired using a Micro-Raman HORIBA XploRA system equipped with an asymmetric crossed Czerny-Turner spectrometer and a back-illuminated CCD camera (1024×256 pixels). The laser beam was focused onto the sample surface using an Olympus 10X microscope objective. Then, spectra were typically acquired over the ranges 200–3600 cm^{-1} and 200–2000 cm^{-1}, with an acquisition time of 2 seconds and 30 accumulations per spectrum. Instrumental parameters included a 100 µm confocal pinhole, a 300 µm slit width, and a 1200 grooves/mm holographic grating. All measurements were conducted at room temperature. The spectrometer was calibrated daily using the 520 cm^{-1} Raman peak of a silicon wafer.

For SERS measurements, 40 µL of the prepared herbicide/KI mixture was deposited onto the ZnO/AuNPs substrate surface. The substrate was then positioned under the Raman microscope objective. Raman spectra were collected from various points on the substrate surface, and subsequent analyses focused on spectra obtained from areas exhibiting the strongest surface-enhanced Raman scattering (SERS) enhancement. Spectral processing was performed using LabSpec6® software.

Calibration curve for glyphosate and glufosinate SERS sensor

The entire calibration curve generation process was performed in triplicate (n = 3), using a fresh SERS sensor for each replicate to assess inter-sensor variability and reliably determine the method's sensitivity. To construct the calibration curves, a baseline Raman spectrum was first acquired from a clean, unused SERS sensor of ZnO/AuNPs. After confirming the absence of contaminants, the sensor surface was moistened with distilled water. The lowest concentration of the target herbicide (e.g., 50 yM) was then deposited onto the moist sensor, and its corresponding SERS spectrum was recorded. The sensor was subsequently rinsed

thoroughly with distilled water. Without allowing the surface to dry completely, the next higher concentration of the herbicide was deposited, and another SERS spectrum was acquired. This sequential process of rinsing, depositing the next concentration, and obtaining the spectrum was repeated for all herbicide concentrations in ascending order, ensuring the sensor remained moist throughout.

Reusability analysis of the SERS sensor

For the reusability test, a sensor was first contaminated by depositing a glyphosate and glufosinate solution (1 µM). The contaminated sensor was then exposed to UV light from a lamp with a peak wavelength of 395 nm (Nicrom B74uV) for 2 and 5 minutes. The efficacy of the cleaning process was evaluated by acquiring Raman spectra after UV exposure and analyzing the presence or disappearance of characteristic herbicide vibrational bands. To assess the repeatability of this cleaning method, the contamination (1 µM glyphosate) and UV cleaning (5 min exposure) protocol was repeated ten times on the same sensor, with Raman spectra acquired after each cleaning cycle.

Real sample analysis using the ZnO/Au SERS substrates

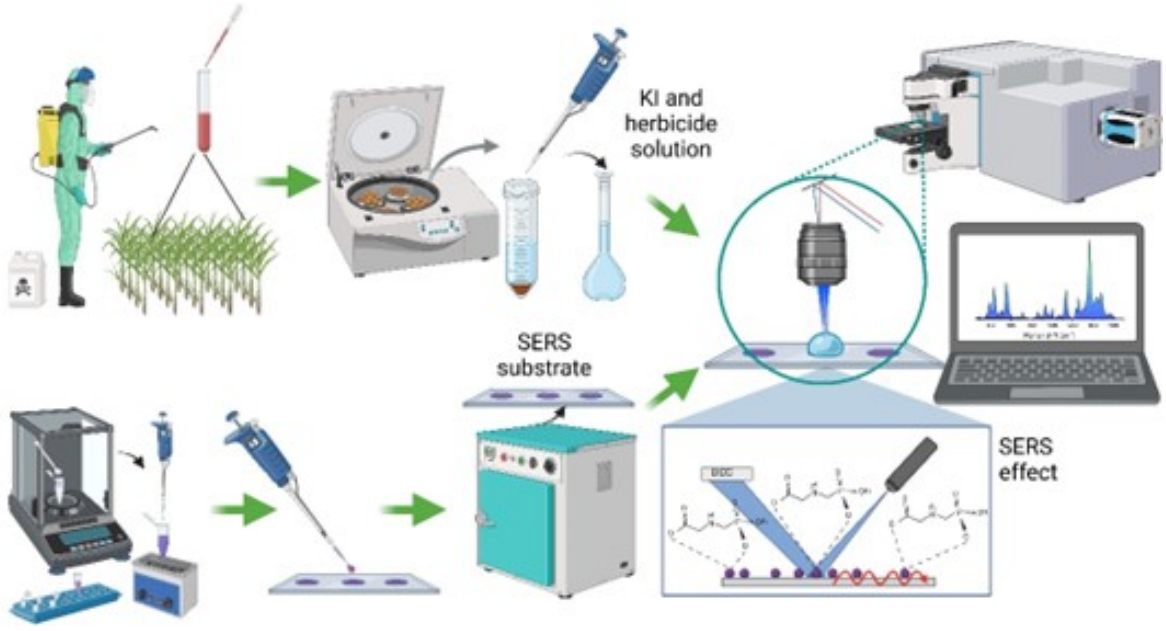

Figure S1. Schematic representation of SERS analysis of herbicides

DISCUSSION AND RESULTS

Surface plasmon and band gap analysis of ZnO/Au nanoparticles

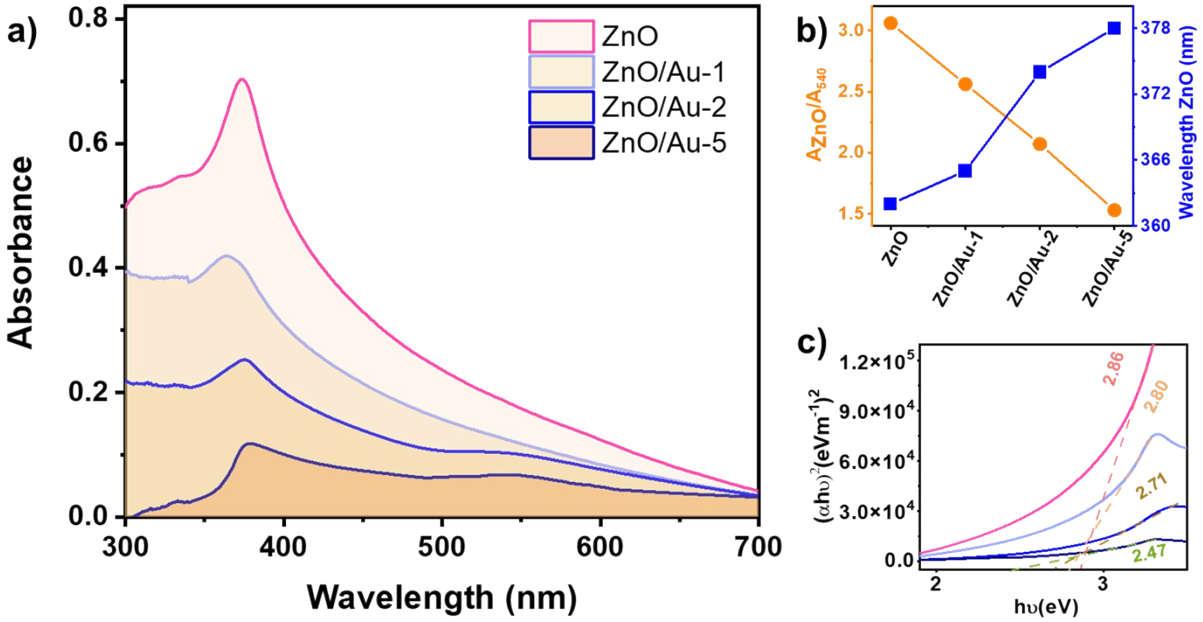

Figure S2. a) UV-Vis spectra from the ZnO NPs and the different concentrations of $HAuCl_4$ salt used for the ZnO/Au NPs, b) ratio from the ZnO absorbance against the 540nm absorbance attributed to the AuNPs and c) Tauc plots used for calculating the bandgap.

Structural characterization of ZnO/Au NPs

Figure S3 presents representative micrographs acquired using secondary electron (SE) and backscattered electron (BSE) imaging in scanning electron microscopy (SEM) mode, as well as bright-field (BF) and dark-field (DF) imaging in scanning transmission electron microscopy (STEM) mode, for the ZnO/Au-1, ZnO/Au-2, and ZnO/Au-5 samples. A systematic increase in the density of Au nanoparticles (AuNPs) is clearly observed from ZnO/Au-1 to ZnO/Au-5, consistent with the increasing Au content in the samples. In both SEM and STEM images, the AuNPs appear as high-contrast features due to the strong atomic-number contrast between Au and ZnO, particularly evident in BSE and DF-STEM images. Importantly, the AuNPs are homogeneously distributed over the ZnO matrix, with no evidence of significant aggregation or phase separation, indicating effective nanoparticle deposition and good interfacial contact between Au and ZnO.

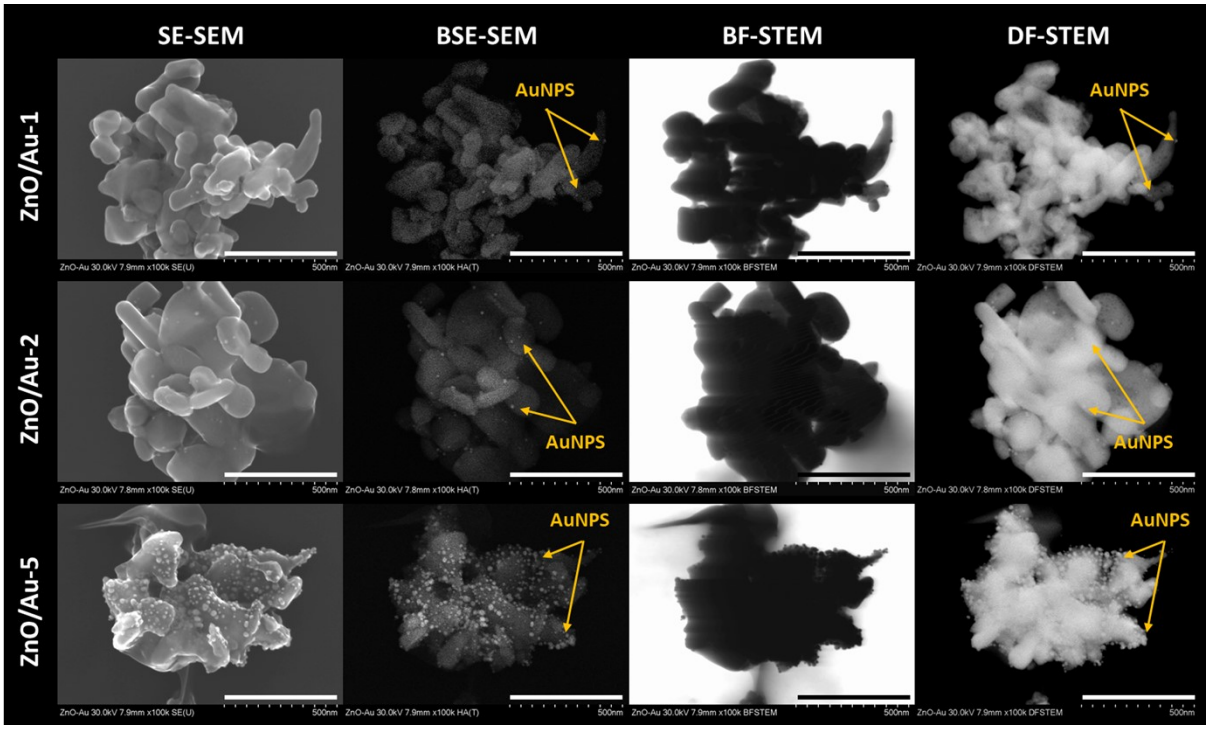

Figure S3. Representative micrographs acquired using scanning electron microscopy (SEM) and scanning transmission electron microscopy (STEM) for the ZnO/Au-1, ZnO/Au-2, and ZnO/Au-5 samples.

On the other hand, the SEM-EDS spectra presented in Figure S4a confirm the presence of the elements Cu, Al, Au, Zn, and O, which are attributed to the ZnO/Au nanoparticles and the sample holder substrate. In the inset, a progressive increase in the intensity of the Au peak is observed as the precursor concentration increases from 1 to 5 mM, indicating more significant nanoparticle deposition and validating the results observed in SEM micrographs. Additionally, elemental mapping for the sample synthesized with 5 mM of Au precursor in Figure S4b reveals the spatial distribution of the elements Zn (red), O (green), and Au (blue), showing a homogeneous coverage of Au on the surface of the ZnO particles. This result confirms the functionalization of ZnO with AuNPs, a crucial aspect of their performance as advanced SERS sensors, which could enhance their performance for herbicidal detection and quantification.

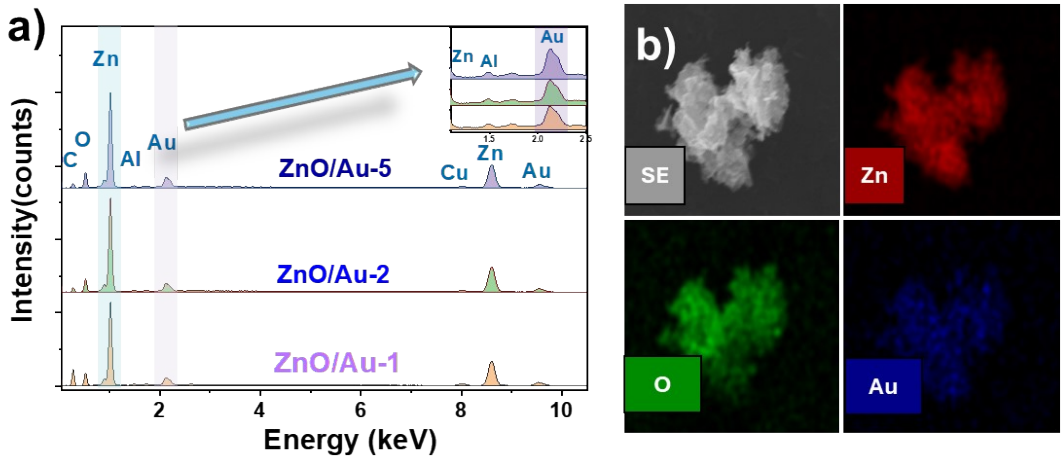

Figure S4. a) EDS chemical analysis of the different nanostructures (ZnO/Au-1, ZnO/Au-2, and ZnO/Au-5) and b) elemental mapping of the ZnO/Au-5 sample.

Table S3. Structural parameters obtained from the refinement of the diffractograms of ZnO samples decorated with AuNPs

	Lattice parameters		Crystal size	wt
	a (nm)	b (nm)	X (nm)	%
ZnO				
ZnO	0.32501	0.52062	47.91	100
Au	---	---	---	---
ZnO/Au-1				
ZnO	0.32503	0.52073	47.12	99.81
Au	0.407	---	42.44	0.19
ZnO/Au-2				
ZnO	0.32502	0.52076	46.93	98.61
Au	0.40673	---	42.83	1.39
ZnO/Au-5				
ZnO	0.32501	0.52078	48.76	85.16
Au	0.40763	---	41.97	14.84

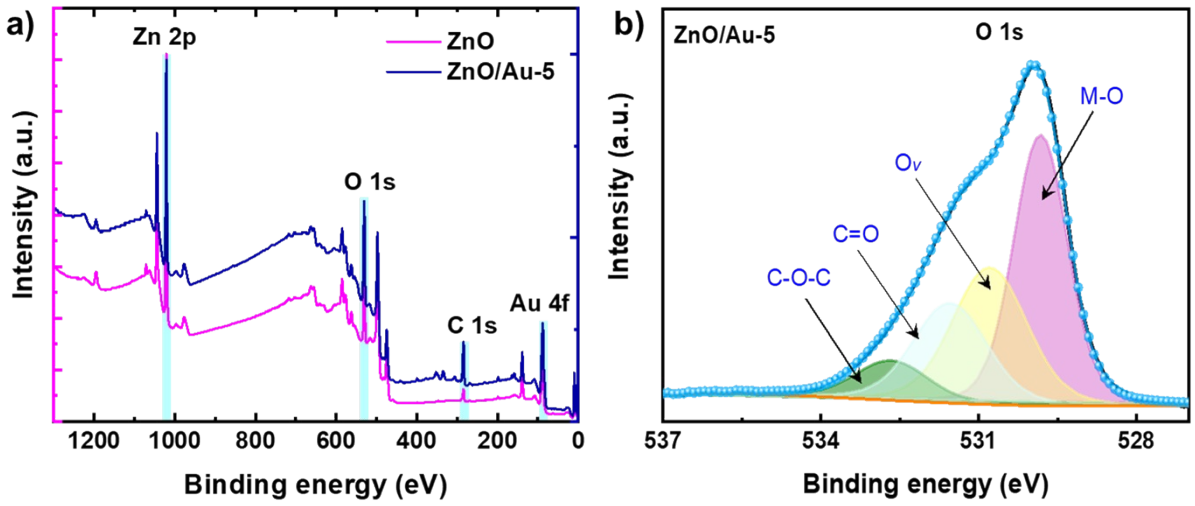

Figure S5. a) XPS survey of ZnO and ZnO/Au-5 and b) Deconvoluted XPS spectra of ZnO/Au-5 for the core levels of O 1s

Regarding the high resolution XPS spectra; as zinc was in the form of oxides, the O-1s spectrum of ZnO/Au-5 (Figure 1e) was deconvoluted into four components: lattice oxygen in ZnO (M-O at 529.81 eV), oxygen vacancies (O_v at 530.78 eV), and contributions from C-O-C (532.66 eV) and C=O (531.53 eV) groups(Chen et al., 2022). The Au-4f spectrum of ZnO/Au-5 (Figure 1f) displayed the Au $4f_{7/2}$ peak at 83.04 eV and the Au $4f_{5/2}$ peak at 86.72 eV, characteristic of metallic gold (Au^0)(Ye et al., 2021). In addition, signals corresponding to Zn-3p states (Zn-$3p_{3/2}$ at 88.1 eV, Zn-$3p_{1/2}$ at 90.61 eV) were also observed in this region(Bharti et al., 2021; Ye et al., 2021). Then, the Zn-2p spectrum (Figure 1g) showed the characteristic doublet for Zn^{2+} in ZnO, with Zn-$2p_{3/2}$ at 1021.01 eV and Zn-$2p_{1/2}$ at 1044.07 eV for pure ZnO, and slightly shifted to 1021.1 eV and 1044.2 eV, respectively, for ZnO/Au-5(Bharti et al., 2021). For gold, the detection of metallic Au^0 is fundamental for the electromagnetic enhancement mechanism in SERS.

FTIR and Raman analysis from derived sargassum ZnO and ZnO/Au NPs

Figure S6a shows the FTIR spectra of the green synthesized ZnO and ZnO/AuNPs using sargassum extract. It's seen that ZnO/Au spectra are quite similar, suggesting that the surface of the nanoparticles is covered with functional groups derived from the extract. However, there are noticeable differences in the spectrum of ZnO, which only shows the typical signal of ZnO around 433-490 cm^{-1} (Zone III), corresponding to the Zn-O bond. In addition, the ZnO/Au samples exhibit hydroxyl compounds, which give rise to the characteristic broad absorption

band between 3650 and 3250 cm^{-1} (Zone I). The signals observed in Zone II at 2923 and 2960 cm^{-1} can be attributed to the symmetric and asymmetric stretching vibrations of the C-H bonds from the CH_2 groups of aliphatic and cyclic compounds. The weak signals at 1737 cm^{-1} can be assigned to the presence of unconjugated carbonyl groups (C=O) resulting from the esterification of lignin (Cachet et al., 2014). The broad band located between 1600 and 1550 cm^{-1} was related to aromatic skeletal vibrations, which are characteristics of phenolic hydroxyl groups (Fodil Cherif et al., 2020; Moubarik et al., 2015). The analyzed samples also showed the presence of olefinic groups, which were detected in the spectra through absorption bands between 1430 and 1410 cm^{-1}. These bands were assigned to vinyl C-H in-plane bending vibrations. The presence of aromatic ethers was also detected in the spectra, which was indicated by the bands around 1250 cm^{-1}. Additionally, the bands at 1099 and 1019 cm^{-1} were attributed to the C-O stretching of primary alcohols (Hussin et al., 2013).

These results suggest that the polyphenolic groups found in sargassum act as the primary stabilizers and reducing agents for the biosynthesis of ZnO/AuNPs. *Sargassum* spp. is an alga that contains a high amount of polyphenol complex or lignin-like materials, as supported by various references (González-Fuentes et al., 2020; López-Miranda et al., 2021a; López-Miranda et al., 2021b). This explains that the different signals attributed to these polyphenolic compounds appear in the FTIR spectra as the concentration of Au synthesized using sargassum extract increases.

Raman spectroscopy was employed to investigate the crystalline structure and vibrational properties of the ZnO and the ZnO/Au NPS materials (Figure S5b). The Raman spectra of ZnO and ZnO/Au materials exhibited characteristic signals of the wurtzite structure (Figure S5b and S6), which was previously confirmed by XRD analysis. For the Raman spectrum of ZnO/Au-5 (Figure S6b), shifts in the ZnO signals are observed, suggesting that the gold nanoparticles cause a slight frequency shift due to defects or lattice strain and an additional frequency at 542 cm^{-1}, which is not typical of pure ZnO and may result from interactions between ZnO and the gold nanoparticles, highlighting the presence of structural defects or alterations in the material's electronic properties. Finally, the C-O-C signal is absent in Au-doped ZnO. These observations suggest that doping with gold nanoparticles affects the structure and properties of ZnO, a phenomenon commonly observed in semiconductor-metal composites(Calzolari and Nardelli, 2013; López-Miranda et al., 2023).

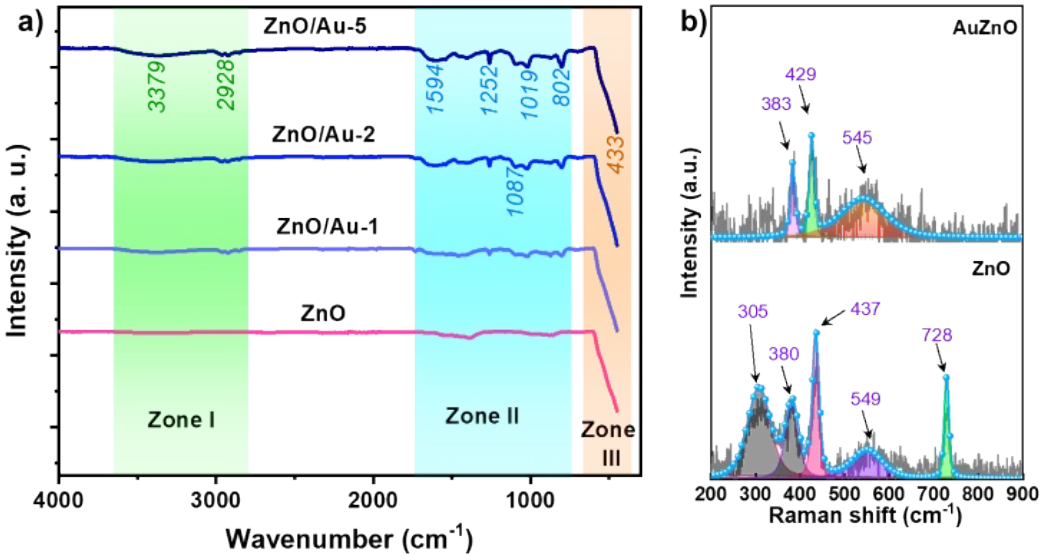

Figure S6. a) FTIR spectra of pristine ZnO nanoparticles and the ZnO/AuNPs with different concentrations of $HAuCl_4$ salt used for the synthesis, and b) deconvoluted Raman spectra at 785 nm for ZnO and ZnO/Au-5.

Raman analysis for the ZnO and ZnO/Au NPs

Briefly, from the ZnO and ZnO/Au-5 signals exhibited for the wurtzite phase, the peak at 307 cm^{-1} corresponds to the E_1 (TO) vibrational mode, one of the crystal's optical transitions, which may be influenced by lattice strain. The signal at 382 cm^{-1} approximates the E_2 (high) mode, typically observed around 437 cm^{-1}; this shift may indicate the presence of surface defects induced by the green synthesis process. The signal at 435 cm^{-1}, assigned to the E_2 (high) mode, is a common optical transition in the wurtzite structure of ZnO and serves as an indicator of good crystalline quality. The signal at 551 cm^{-1} is atypical in the Raman spectrum of pure ZnO and may suggest the presence of structural defects, dopants, or impurities that alter the material's properties. Finally, the signal at 729 cm^{-1} is associated with the presence of the C-O-C group, likely originating from organic matter or the Zn salt precursor.

In the Raman spectrum of ZnO/Au-5, shifts in the ZnO signals are observed: the first at 384 cm^{-1}, near the ZnO E_2 (high) mode, indicating the influence of gold nanoparticles on the crystal lattice; at 426 cm^{-1}, also related to the E_2 (high) mode, suggesting that the gold nanoparticles cause a slight frequency shift due to defects or lattice strain.

Similarly, the Raman spectra of ZnO/Au-1 and ZnO/Au-2 nanoparticles (Figure S7) also displayed signals characteristic of a wurtzite-type structure. However, key ZnO signals (around 320, 437, and 555 cm^{-1}) generally exhibited lower intensities in these samples. Notably, in the

ZnO/Au-2 spectrum, the peak at approximately 555 cm^{-1} was observed with significant intensity relative to its other features. When these materials were evaluated as SERS sensors for glyphosate, ZnO/Au-1 exhibited no discernible SERS effect at a 25 µM concentration of glyphosate. In contrast, ZnO/Au-2 showed a weak SERS response to glyphosate, with only two signals at 1255 and 1370 cm^{-1}. These preliminary SERS results for ZnO/Au-1 and ZnO/Au-2 highlight differences in SERS activity related to variations in Au nanoparticle deposition or characteristics and provide a contrast to the more effective ZnO/Au-5 material, details of which are described subsequently.

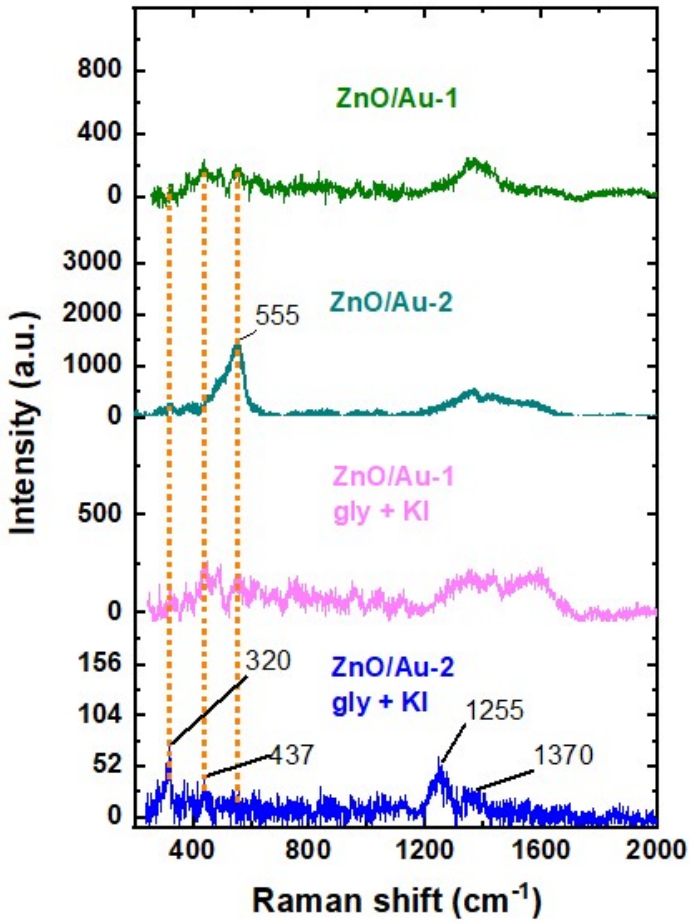

Figure S7. Raman spectra of ZnO/Au-1, ZnO/Au-2, and of the interaction between ZnO/Au NPs and herbicides in KI solution

FTIR, Raman and DFT calculation analysis of herbicides

Figure S8a shows the FTIR spectra of glufosinate and glyphosate. The characteristic vibrations of each molecule are highlighted in the color rectangles. The symmetrical and asymmetric stretching of the -CH_2 bonds were identified between 3000 and 3647 cm^{-1}. The vibrations attributed to -OH and -NH stretching were identified between 3100 and 3600 cm^{-1}.

Additionally, the bands in 1700 and 1650 cm^{-1} were related to the presence of -C=O bonds. The characteristic bands assigned to the stretching of P-OH and P=O bonds from the phosphate group were identified around 900 to 100 cm^{-1} and 100-1290 cm^{-1}, respectively. Finally, those corresponding to the carboxylate group (-CO-O-) and C-N bonds were found between 1300 and 1570 cm^{-1}. Both molecules exhibit similar bands; however, due to the differences in their chemical structures, the intermolecular interactions affect the shape and position of the FTIR bands. Mainly, this is observed in the bands attached to the NH, where glufosinate shows two distinct bands around 3060 and 3200 cm^{-1}, compared with glyphosate, which has less defined bands due to the presence of a primary amine in glufosinate and a secondary amine in glyphosate. In addition, these primary and secondary amines exhibit flexion bands around 1550-1555 and 1570-1650 cm^{-1}, respectively.

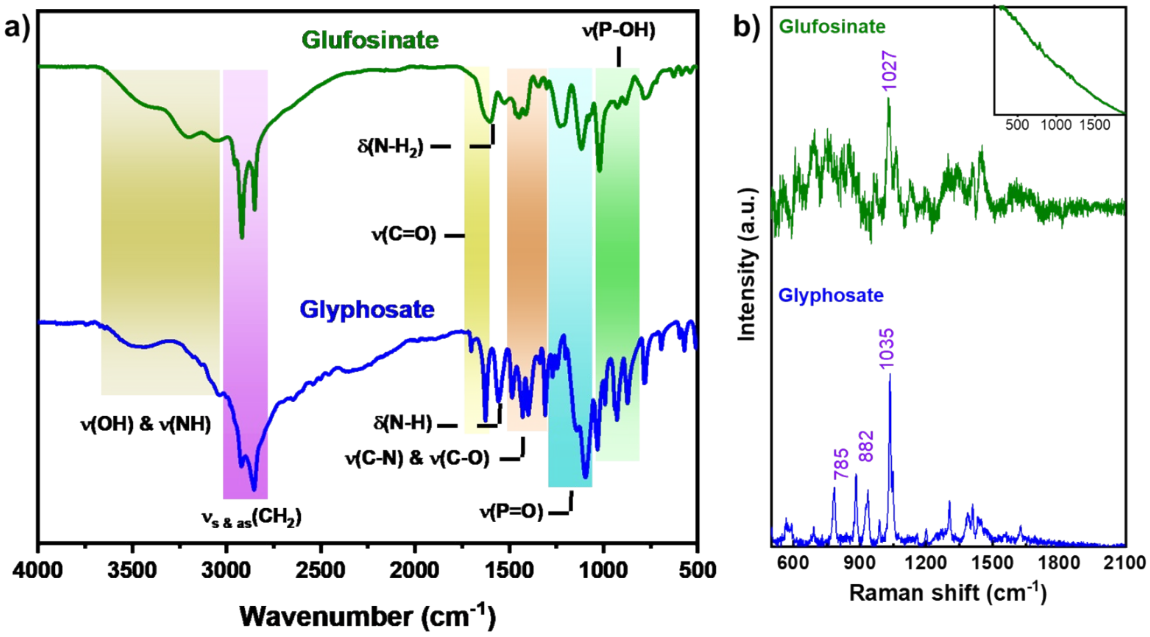

Figure S8. a) FTIR and b) Raman spectra of ammonium glufosinate and glyphosate.

The Raman spectrum of pure glyphosate at 785 nm (Figure S8b, S11a-b.) reveals several signals associated with the characteristic molecular vibrations of this compound. To provide a more detailed assignment of these Raman shifts and facilitate comparison with the SERS spectra, the glyphosate Raman spectrum was deconvoluted (Figures S11a-b). The resulting Raman shifts and their assignments are summarized in Table S6. The peak at 306 cm^{-1} likely corresponds to C–C bond vibrations, while those at 326 and 350 cm^{-1} may be associated with skeletal C–C or C–N vibrations. The signals at 486 and 579 cm^{-1} are probably related to

phosphonate (P–O) group deformations. The band at 688 cm^{-1} is typically attributed to C–P bond vibrations, a distinctive feature of glyphosate (Holanda et al., 2020). Signals at 783 and 882 cm^{-1} can be assigned to C–H group vibrations and the molecular backbone. The signal at 932 cm^{-1} is associated with P–O stretching, while the band at 989 cm^{-1} may indicate deformations in the P–OH bond. In the mid-frequency region, the peak at 1034 cm^{-1} and bands at 1154, 1258, and 1305 cm^{-1} are associated with C–N stretching vibrations and the carboxylate group. The signals at 1388 and 1408 cm^{-1} are generally attributed to C–H bending vibrations. The intense band at 1450–1469 cm^{-1} is linked to C–H bending vibrations in methyl groups. In contrast, signals at 1554 and 1624 cm^{-1} are characteristic of C=O stretching in the carboxylic group and conjugated C=C or C=N bonds (Holanda et al., 2020).

On the other hand, the Raman spectrum of ammonium glufosinate exhibited a significant fluorescence effect when using the 785 nm laser, even at low power levels (Figure S8b and Figure inset). To analyze the spectrum, baseline correction was applied, and deconvolution was performed in the 1000-1800 cm^{-1} range (Figure S11c-d), as analysis at lower Raman shifts was challenging due to the strong fluorescence overlapping the signals. According to DFT simulations and limited literature (Hu et al., 2022), the band at 1035 cm^{-1} is likely associated with P-O symmetric stretching modes of the phosphinate group. It may also include contributions from C-N stretching. The band at 1071 cm^{-1} could be attributed to asymmetric P-O stretching of the phosphinate group, further C-N stretching, or vibrational modes involving the ammonium counterion. The signal at 1127 cm^{-1} corresponds well with C-N symmetric stretching. In the mid-frequency region, bands at 1301 cm^{-1} and 1354 cm^{-1} are characteristic of -CH_2- deformation modes (such as twisting or wagging) and potentially NH_2 group deformations. The band observed at 1406 cm^{-1} can be assigned to -CH_2- scissoring and, significantly, for the ammonium salt form, the symmetric stretching of the carboxylate (COO^-) group. The subsequent band at 1455 cm^{-1} also falls within the -CH_2- scissoring and C-H deformation region and may additionally include contributions from deformation modes of the ammonium (NH_4^+) ion or other amine-related vibrations (Table S7). Finally, the prominent band at 1603 cm^{-1} is characteristic of the asymmetric stretching of the carboxylate (COO^-) group, which is expected for ammonium glufosinate. This region can also contain signals from NH_2 or NH_3^+ deformation modes.

Additionally, a quantum-mechanical atomistic simulation method, such as a density functional theory (DFT) analysis calculation for glyphosate and glufosinate, was performed to provide a

reference for comparison between the experimental FTIR and Raman spectra. For this, the geometry of glyphosate and glufosinate were fully optimized using the B97 (augmented with D3 correction) using water as the solvent for the Self-Consistent Reaction Field (SCRF) with the Solvation Model based on Density (SMD); the basis set 6-311g(d,p) was used, and the simulation conditions were maintained every re-optimization step, assuming an ultrafine numeric integration cell with no symmetry restrictions and temperature set at 273K. The geometrically optimized structures for glyphosate are shown in Figure S9a and for glufosinate in Figure S9b.

After the DFT calculation, the GaussSum software (O'Boyle et al., 2008) was used for specific corrections: a temperature of 298 K was set for both the FTIR and Raman spectra, and a 785 nm wavelength correction was applied to the Raman spectra. Once the calculations were corrected, the data were extracted, and the absorbance spectra for both FTIR and Raman were plotted, as observed in Figure S9c and Figure S9d.

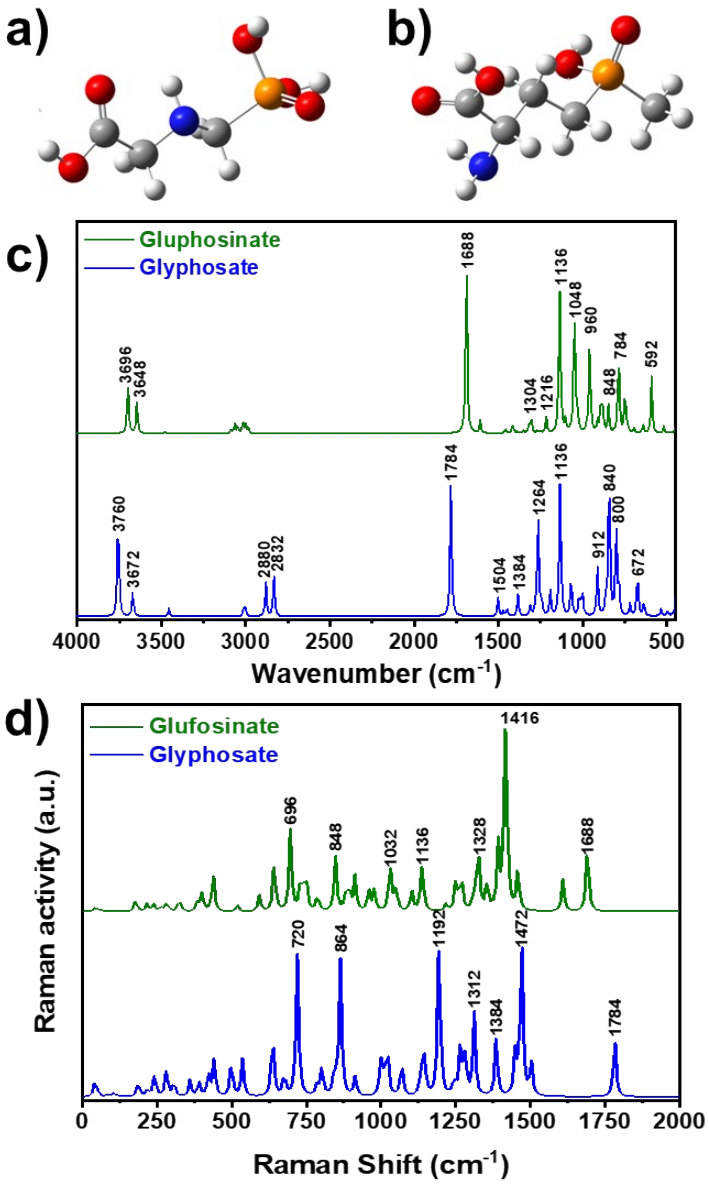

Figure S9. Optimized structure of a) glyphosate and b) ammonium glufosinate. DFT simulated spectra of ammonium glufosinate and glyphosate: c) FTIR and d) Raman.

The tables of comparison between the experimental and theoretical for both FTIR and Raman spectra of each herbicide, glyphosate, and glufosinate can be observed hereafter:

Table S4. Comparison of experimental and DFT-calculated FTIR bands for glyphosate

Herbicide	**Wavelength (cm^{-1})**	**Assignment**	**Wavelength (cm^{-1})**	**Assignment**
	Experimental		**DFT**	
	---	---	592	C-H rocking
	694	C-C stretching	---	---
	873	P-O stretching	784	C-P-O asymmetric stretch
	---	---	848	P-O-H asymmetric stretch
	---	---	888	C-H rocking
	---	---	960	C-H rocking
	992	C-O stretching	---	---
	1032	C-N stretching	---	---
	---	---	1048	C-H symmetric stretch
Glyphosate	1096	P-O bending	---	---
	---	---	1136	C-N symmetric stretch
	---	---	1216	C-H twisting
	1310	C-H deformation	1304	C-H and O-H wagging
	1429	C-O-H bending	---	---
	1626, 1702	C=O stretching	1688	C=O symmetric stretch
	2854	C-H symmetric stretching	---	---
	2921	C-H asymmetric stretching	---	---
	3479	O-H symmetric stretching	3648, 3696	O-H symmetric stretch

Table S5. Comparison of experimental and DFT-calculated FTIR bands for glufosinate

Herbicide	Wavelength (cm^{-1})	Assignment	Wavelength (cm^{-1})	Assignment
	Experimental		**DFT**	
Ammonium Glufosinate	---	---	672	C-P-O symmetric stretch
	725	P-O stretching	---	---
	---	---	800	C-P-O asymmetric stretch
	---	---	840	C-N asymmetric stretch
	---	---	912	C-C asymmetric stretch
	928	C-O stretching	---	---
	1022	O-P-O symmetric stretching	---	---
	1117	O-P-O asymmetric stretching	---	---
	---	---	1136	C-O & C-N asymmetric stretch
	1230	P=O stretching	---	---
	---	---	1264	C-H bending
	---	---	1384	C-H & N-H rocking
	1447	O-C-O symmetric stretching	---	---
	---	---	1504	N-H scissoring
	1602	O-C-O asymmetric stretching	---	---
	---	---	1784	C-O asymmetric stretch
	2851	C-H symmetric stretching	2832, 2880	C-H symmetric stretch
	2919	C-H asymmetric stretching	---	---
	3050	NH3+ stretching from amine salt	---	---
	3200	C=O stretching overtone	---	---
	---	---	3672, 3760	O-H stretching

Table S6. Comparison of experimental at 785 nm and DFT-calculated Raman bands for glyphosate

Herbicide	Raman Shift (cm^{-1})	Assignment	Raman Shift (cm^{-1})	Assignment
	Experimental		**DFT**	
Glyphosate	306	C–C bond vibrations	---	---
	326, 350	Skeletal C–C or C–N vibrations	---	---
	486, 579	Phosphonate (P–O) group deformations	---	---
	688	C–P bond vibrations	720	P-C symmetric stretching
	783	C–H group vibrations and molecular backbone	---	---
	882	C–H group vibrations and molecular backbone	864	$-CH_2-$ rocking
	932	P–O stretching	---	---
	989	Deformations in the P–OH bond	---	---
	1034	C–N stretching vibrations and the carboxylate group	---	---
	1154	C–N stretching vibrations and the carboxylate group	1192	$-CH_2-$ twisting
	1258, 1305	C–N stretching vibrations and the carboxylate group	1312	$-CH_2-$ wagging
	1388, 1408	C–H bending vibrations	1384	$-CH_2-$ wagging
	1450–1469	C–H bending vibrations in methyl groups	1472	$-CH_2-$ symmetric stretching
	1554, 1624	C=O stretching in the carboxylic group and conjugated C=C or C=N bonds	1784	C=O symmetric stretching

Table S7. Comparison of experimental at 785 nm and DFT-calculated Raman bands for ammonium glufosinate

Herbicide	Raman Shift	Assignment	Raman Shift	Assignment

	(cm⁻¹)		(cm⁻¹)	
	Experimental		**DFT**	
Ammonium Glufosinate	~1035	P-O symmetric stretching (phosphinate), C-N stretching	1032	P-O symmetric stretching
	~1071	Asymmetric P-O stretching (phosphinate), C-N stretching, ammonium modes	-	-
	~1127	C-N symmetric stretching	1136	C-N symmetric stretching
	~1301	-CH_2- & NH_2 twisting/deformation	1328	-CH_2- & NH_2 twisting
	~1354	-CH_2- & NH_2 twisting/deformation, C-H bending		
	~1406	-CH_2- scissoring, Symmetric COO^- stretching	1416	-CH_2- scissoring
	~1455	-CH_2- scissoring, C-H deformations, Ammonium (NH_4^+) / Amine (NH_3^+) deformations		
	~1603	Asymmetric COO^- stretching, NH_2 /NH_3^+ deformations	1688	C=O symmetric stretching (from COOH form in DFT)
	---	---	848	C-C & C-N symmetric stretching
	---	---	696	P-C symmetric stretching

Control Experiments and Substrate Interaction

Control experiments were conducted to elucidate the interactions between the substrate, solvent (water), and the KI agent (Figures S10a and S10b). Raman spectra of ZnO and ZnO/Au-5

substrates immersed in water showed the expected substrate peaks. Upon addition of the KI solution to ZnO/Au-5, slight modifications in the ZnO-related bands were observed (peaks shifting to ~380, 422, 564 cm^{-1}), potentially indicating the interaction of iodide ions with the substrate surface or induced changes in the ZnO structure near the AuNPs(Song et al., 2022).

Crucially, when glyphosate or ammonium glufosinate (at 25 µM concentration with KI) was added to the reference ZnO substrate (lacking Au), only signals corresponding to ZnO (~380, 435 cm^{-1}) and possible carbonate/C-H residues (~729, 1059 cm^{-1}) were detected. No characteristic signals from the herbicides themselves were observed under these conditions. This confirms that the presence of gold nanoparticles is essential for achieving the SERS effect and detecting herbicides at these concentrations. This confirms the primary role of the plasmonic effect (electromagnetic enhancement) originating from the AuNPs in achieving the SERS signal, excluding secondary contributions from the ZnO (charge transfer)(Cong et al., 2020)

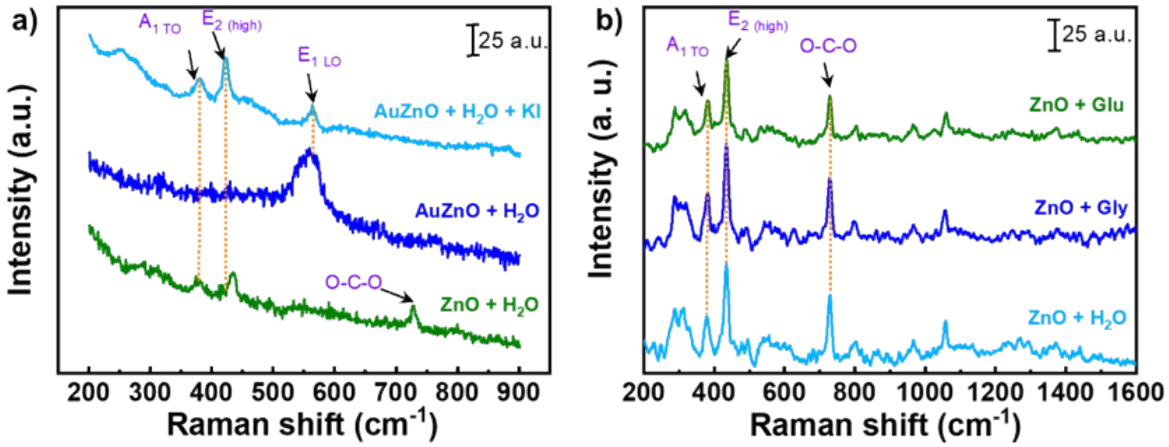

Figure S10. a) Interaction of solvent and KI solution with substrates, and b) interaction of herbicides with ZnO substrates

SERS sensor detection of herbicides

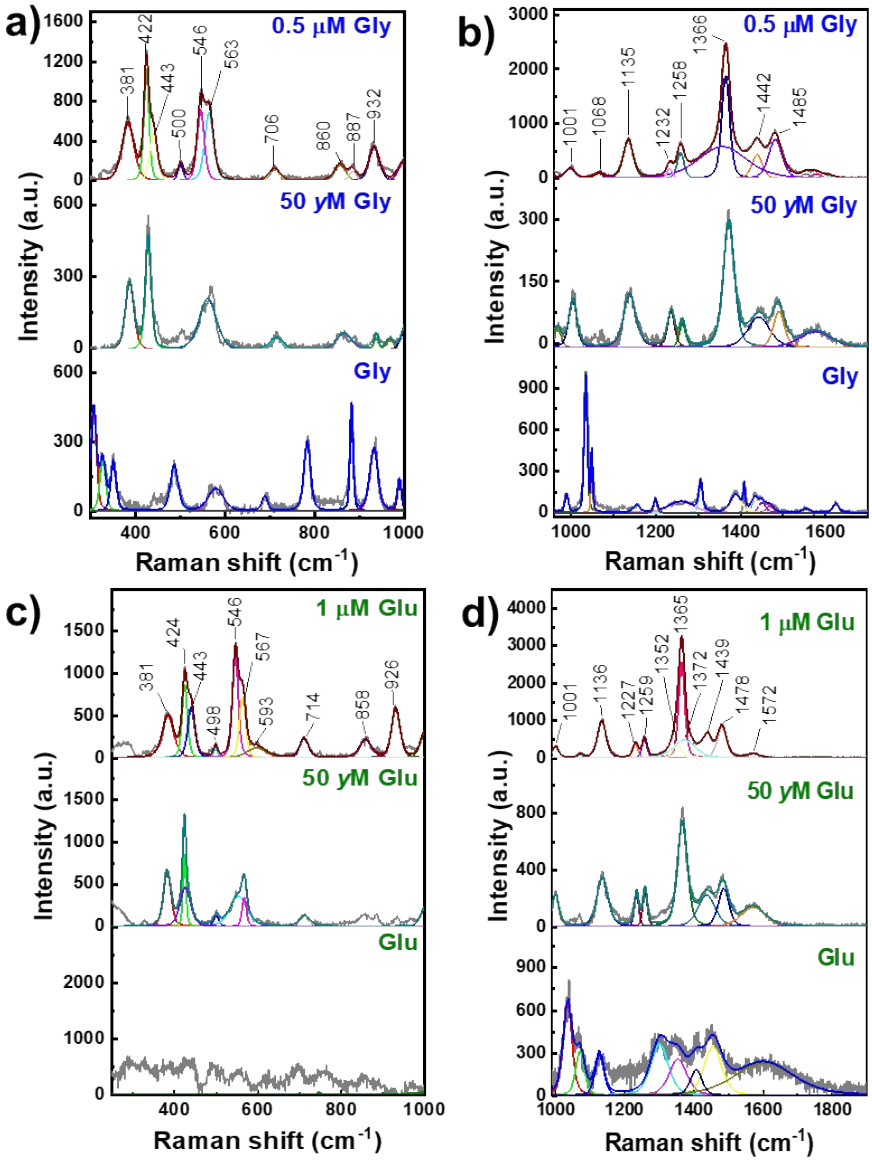

Figure S11. Deconvoluted SERS spectrum of a-b) glyphosate and c-d) glufosinate in KI solution in ZnO/Au-5 substrates at 785 nm.

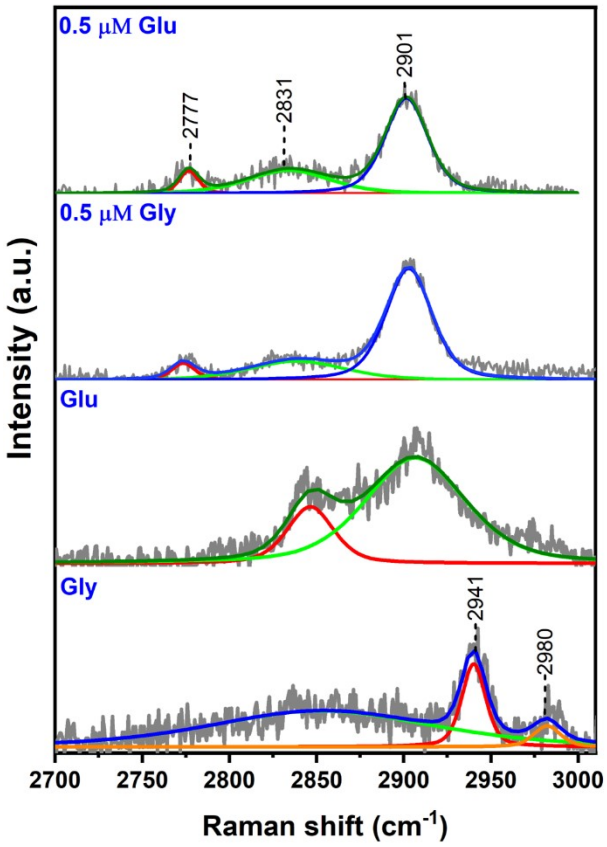

Figure S12. Deconvoluted SERS spectrum of glyphosate and glufosinate in KI solution in ZnO/Au substrates at 785 nm at high frequencies.

Details on SERS Enhancement Factor (EF) Calculation

The Enhancement Factor (EF) is a crucial metric in Surface-Enhanced Raman Scattering (SERS) spectroscopy, quantifying the signal amplification achieved when an analyte is adsorbed onto a SERS-active surface compared to its normal Raman signal. This factor serves as a direct measure of a SERS substrate's efficiency and enables performance comparison across different platforms. Essentially, a high EF indicates the capability to detect significantly lower analyte concentrations, which is fundamental for ultrasensitive applications(Cara et al., 2020).

To quantify the Raman signal enhancement provided by the ZnO/Au-5 substrates, the SERS Enhancement Factor (EF) was calculated using the following general equation:

$$EF = \left(\frac{I_{SERS}}{I_{Raman}}\right)\left(\frac{C_{Raman}}{C_{SERS}}\right) \quad (1)$$

Where I_{SERS} is the intensity of a characteristic band from the SERS spectrum of the analyte on the ZnO/Au-5 substrate, and C_{SERS} is the analyte concentration in the SERS measurement. For normal Raman measurements, I_{Raman} is the intensity of the same characteristic band obtained from the Raman spectrum of the pure analyte, and C_{Raman} is the analyte concentration in the normal Raman measurement.

Given the inability to observe characteristic herbicide signals at micromolar concentrations on the pristine ZnO substrate (without gold nanoparticles) by conventional Raman spectroscopy, the Raman spectra of 1 M of glyphosate and 1 M of glufosinate were utilized as references for I_{Raman}. For glyphosate, the band at 1387 cm^{-1} with an intensity of 132 a.u. was taken as I_{Raman}. For glufosinate, the band at 1400 cm^{-1} with an intensity of 185 a.u. was used as I_{Raman}. A concentration of 1 M was used for the analytes (C_{Raman}), which is a common practice for EF estimation in cases where the normal Raman signal is weak at lower concentrations. The SERS intensities (I_{SERS}) and SERS concentrations (C_{SERS}) correspond to measurements performed at 50 yM for both herbicides: specifically, around the 1370 cm^{-1} band with an intensity of 2208.66 a.u. for glyphosate and 788 a.u. for glufosinate.

Thus, the calculated SERS enhancement factors were 3.35×10^20 for glyphosate and 8.51×10^19 for glufosinate, underscoring the extreme sensitivity achieved through the engineered surface properties.

Stability of SERS Band Positions and Quantitative Detection Limits

A crucial aspect of the reliability of qualitative and quantitative SERS analysis is the stability of spectral band positions. In this study, experiments for constructing calibration curves were

performed in triplicate, allowing for an assessment of consistency in the Raman shifts of the characteristic SERS bands used for glyphosate and glufosinate. This stability analysis covered the wide range of concentrations investigated, from micromolar levels down to traces in the yM order. As illustrated in Figures S13a (for glyphosate) and S13b (for glufosinate), the positions of these key bands remained remarkably stable. The observed variation in Raman shifts for the main analytical signals were minimal, generally fluctuating within a range of ±0.6 cm^{-1} to ±4.9 cm^{-1} across all studied concentrations. This consistency underscores the stable nature of the analyte-substrate interactions on the ZnO/Au-5 platform. It reinforces the suitability of these bands for unequivocal identification and precise quantification of herbicides.

Importantly, the positions (Raman shifts) of the main SERS bands for both analytes remained constant across the entire tested concentration range, indicating stable analyte-substrate interactions. This stability is crucial for reliable qualitative identification and quantitative analysis. Detection of both herbicides was achieved down to picomolar concentrations, potentially femtomolar or even yoctomolar, far exceeding the capabilities of conventional Raman spectroscopy on pure ZnO.

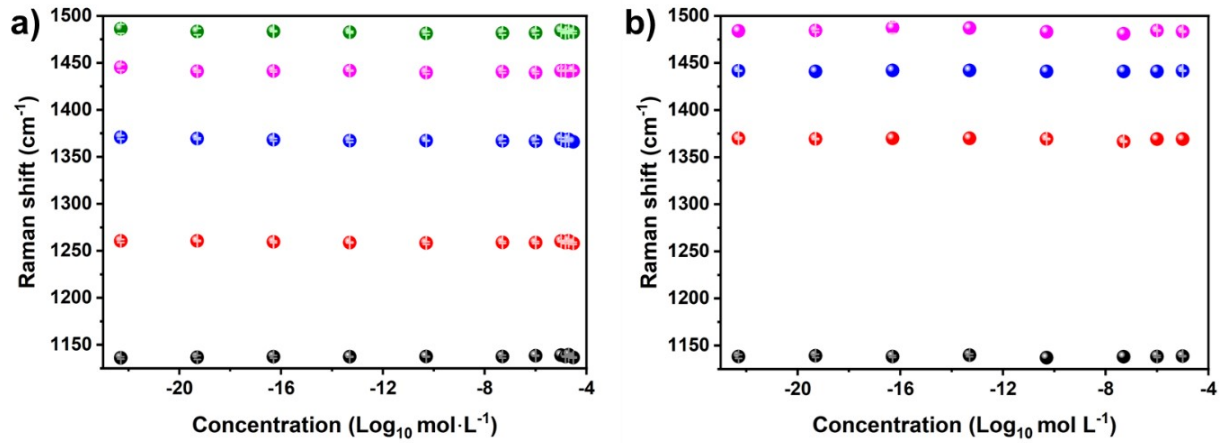

Figure S13. The stability of characteristic Raman peak positions across concentrations for a) glyphosate and b) ammonium glufosinate.

The intensity of several characteristic SERS bands for both glyphosate and glufosinate showed a clear dependence on herbicide concentration. For glyphosate, two calibration regimes were observed. Above 1 μM (Figure S14a), the intensities of the bands at 1370, 1440, and 1486 cm^{-1} exhibited a reasonably linear relationship with concentration (R^2 values ranging from 0.89 to 0.97, see Table S9). The band at 1370 cm^{-1} showed the highest sensitivity in this range. Below 1 μM (down to 50 yM), a linear relationship was observed when plotting intensity versus the logarithm (Log_{10}) of the concentration. The band at 1370 cm^{-1} remained highly sensitive, and the bands at 1138, 1260, 1440, and 1486 cm^{-1} also showed good linearity (R^2 values from 0.95 to 0.99) in this log-linear range. These findings suggest that multiple bands can be used for identification, and specific bands (especially 1370 cm^{-1}) are suitable for quantitative analysis over a very wide dynamic range. The existence of two distinct calibration regimes (linear and log-linear) for glyphosate demonstrates the sensor's capability to quantify over an exceptionally broad dynamic range. The log-linear behavior at ultra-low concentrations is often characteristic of highly sensitive SERS platforms where signal saturation might occur at higher concentrations, suggesting different adsorption mechanisms or saturation kinetics across the concentration range.

For glufosinate, similar concentration-dependent trends were observed (Table S8). The bands at 1138, 1370, 1441, and 1484 cm^{-1} showed increasing intensity with concentration (Figure S14b). Plotting intensity versus Log_{10}(concentration) revealed linear trends, particularly for the bands at 1138 cm^{-1} (R^2 = 0.97) and 1370 cm^{-1} (R^2 = 0.97). This indicates potential for quantitative detection of glufosinate at low concentrations as well.

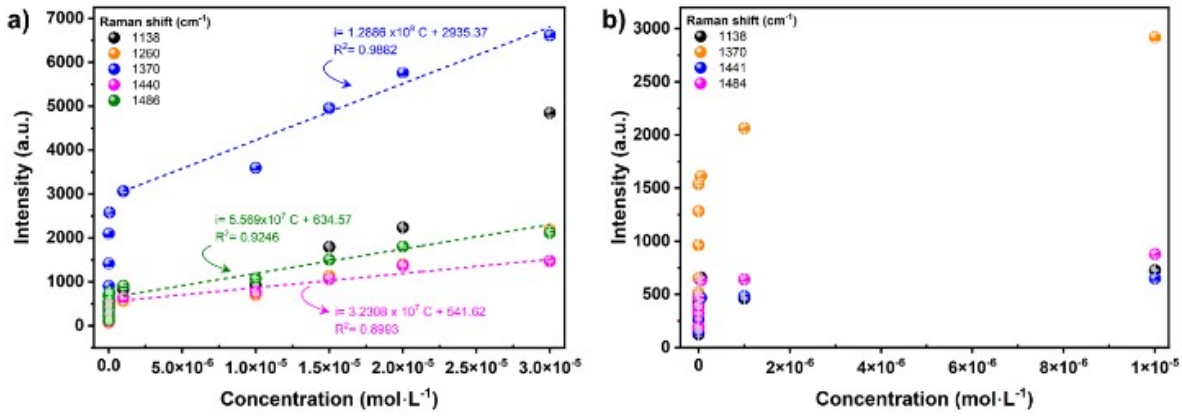

Figure S14. a) Linear calibration curve for glyphosate (1 to 30 µM), and b) Concentration-dependent SERS intensity response for glufosinate (50 yM to 10 µM).

Table S8. Summary of observed SERS bands for glyphosate and glufosinate on the ZnO/Au-5 sensor at 785 nm.

Raman Shift (cm^{-1})	Assignment	Source
307	E1(TO) vibrational mode	ZnO
382, 384, 386	E2(high) mode (shifted)	ZnO, Au-doped ZnO
423, 426, 428	E2(high) mode (shifted)	Au-doped ZnO
435, 439	E2(high) mode	ZnO
542	Interactions between ZnO and gold nanoparticles	Au-doped ZnO
551	Structural defects, dopants, or impurities	ZnO
561, 563	Phosphonate (P-O) group deformation, P-O stretching	Glyphosate
688, 709, 714	C-P bond vibration	Glyphosate
729	C-O-C group	ZnO
783, 882, 856, 865, 884	C-H group vibration, molecular backbone	Glyphosate
932, 938	P-O stretching	Glyphosate
989	P-OH bond deformation	Glyphosate
997, 1004, 1036	C-N stretching, carboxylate group	Glyphosate
1035, 1071	C-N stretching, phosphate or ammonium group deformation	Ammonium glufosinate
1065	C-N stretching, carboxylate group	Glyphosate
1127	C-O bond vibration	Ammonium glufosinate
1134, 1138	C-N stretching, carboxylate group	Glyphosate
1232, 1236, 1258	C-H bending vibration (methyl group)	Glyphosate
1301	Carboxylate group stretching	Ammonium glufosinate
1354, 1455	C-H bending vibration (methyl or methylene group)	Ammonium glufosinate
1357, 1364, 1372,	C-H bending vibration	Glyphosate,

1388, 1406, 1408		Ammonium glufosinate
1438, 1443, 1450-1469	C-H bending vibration (methyl group)	Glyphosate
1554, 1624	C=O stretching (carboxylic group), conjugated C=C or C=N bond	Glyphosate
1577, 1579	C=O stretching (carboxylic group)	Glyphosate
1603	C=O stretching (carboxyl group) or C=C bond	Ammonium glufosinate

Table S9. Quantitative SERS calibration parameters for glyphosate detection

Characteristic SERS band (cm^{-1})	Concentration range (µM or Log_{10}(M))	Regression model	R^2 Value	Slope (Sensitivity)	Intercept
1370	1–30 µM	Linear	0.99	1.289×10^8	2935.37
1440	1–30 µM	Linear	0.89	3.231×10^7	541.62
1486	1–30 µM	Linear	0.92	5.569×10^7	634.57
1370	50 yM–0.1 µM	Log-linear	0.99	149.46	3620.06
1138	50 yM–0.1 µM	Log-linear	0.99	42.23	1062.62
1260	50 yM–0.1 µM	Log-linear	0.99	28.45	705.18
1440	50 yM–0.1 µM	Log-linear	0.99	32.19	825.70
1486	50 yM–0.1 µM	Log-linear	0.99	43.55	1095.29

Table S10. Quantitative SERS calibration parameters for glufosinate detection

Characteristic SERS band (cm^{-1})	Concentration range (µM or Log_{10}(M))	Regression model	R^2 Value	Slope (Sensitivity)	Intercept
1370	50 yM–1 µM	Log-linear	0.98	83.06	2326.18
1441	50 yM–1 µM	Log-linear	0.97	20.12	587.97

Raman and SERS analysis of interferents (atrazine and paraquat)

After baseline treatment, the Raman spectrum of atrazine revealed characteristic bands at 322, 368, 414, 544, 646, 684, 863, 921, 962, 991, 1247, 1443, 1545, and 1956 cm^{-1}. Many of these bands align with previously reported normal Raman and SERS spectra of atrazine (Albarghouthi et al., 2022; Tang et al., 2019; Zanasi et al., 2021). For instance, prominent atrazine SERS signals are documented at approximately 323-326 cm^{-1} (C-Cl stretch), 656-683 cm^{-1} (ring modes), 921 cm^{-1} (CH_3 twisting), 962 cm^{-1} (ring breathing, C-C stretching), 990-1001 cm^{-1} (combination ring mode, NH bending, CN stretching), 1250 cm^{-1} (ring mode, CH_2 twisting), and 1446 cm^{-1} (CH_2 bending). Weaker signals around 1549 cm^{-1} (ring mode and NH bending) and 1602 cm^{-1} (NH bending and CN stretching) are also characteristic. The SERS

signal for atrazine can be highly dependent on the adsorption orientation and the nature of the metallic substrate and previously reported SERS signals for atrazine show some variability.

In contrast, Paraquat analysis on the ZnO/Au-5 sensor was characterized by strong fluorescence, which allowed for the detection of only a few bands at 862, 1211, 1322, and 1671 cm^{-1}. The issue of high fluorescence from complex samples or from paraquat itself, obscuring SERS signals, has been previously noted (Kamkrua et al., 2023; Qiu et al., 2025; Singh et al., 2023). Characteristic SERS bands for paraquat are well-documented and include signals around 674 cm^{-1} (ring deformation), 838-840 cm^{-1} (C-N stretching), 1190-1194 cm^{-1} (C-C bending), 1296-1300 cm^{-1} (C-C structural distortion), 1536 cm^{-1} (ring stretching), and 1645-1671 cm^{-1} (C=N stretching), which generally corroborates the bands observed in this study. The SERS spectra of atrazine and paraquat, obtained from ten replicate analyses using the ZnO/Au-5 sensor, were then compared with those of glyphosate and glufosinate at a concentration of 25 µM.

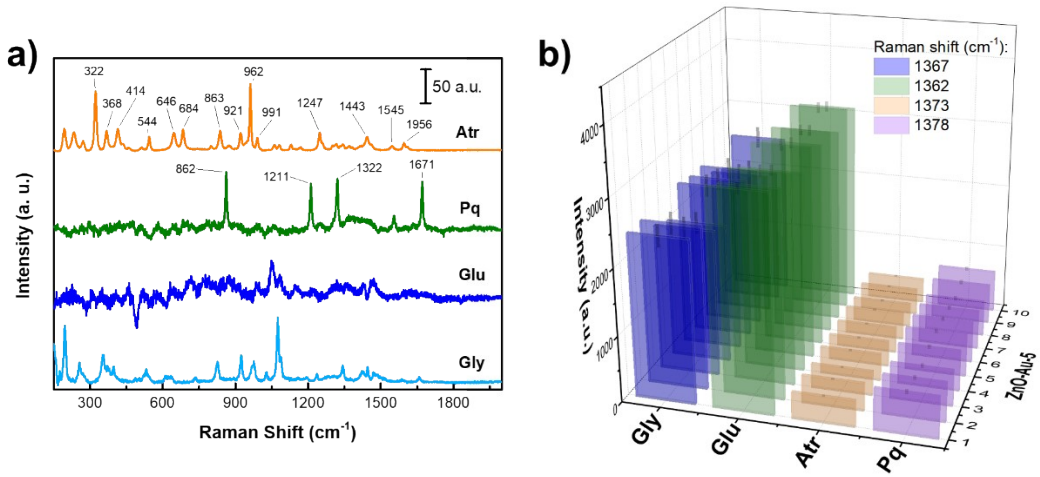

Figure S15. a) Raman spectra of the commercial glyphosate, glufosinate, atrazine, and paraquat. b) Comparative analysis of the SERS signals in a common spectral region (~1370 cm^{-1}) for the four herbicides on the ZnO/Au-5 sensor.

Table S11. Experimental SERS Band Assignments for Pure Herbicides and Binary Mixtures

Herbicide assignment	Pure Standard (RS / w)	Mix with Glyphosate (Rs / w)	Mix with Glufosinate (Rs / w)
Glyphosate			
P-O / C-P stretch	932.6 (28.1)	--	944.4 (18.3)
C-N / carboxylate	997.5 (27.4)	--	1011.1 (16.8)
P-O def / C-N sym	1134.5 (27.5)	--	1144.4 (36.1)
Glufosinate			
P-O sym / C-N	1072.0 (18.5)	1079.7 (18.2)	--
C-N sym / P-O def	1133.7 (29.6)	1144.4 (36.1)	--
Paraquat			
C-C / C-N stretch	1269.5 (10.2)	1271.1 (26.5)	1268.3 (17.5)
Ring C=C / C=N	--	1643.6 (15.1)	1645.1 (13.2)
C-H bending	--	1189.4 (15.7)	1190.9 (4.9)
Atrazine			
Ring breathing	1003.2 (16.6)	1013.2 (15.4)	1011.9 (19.9)
C-N stretching	1126.1 (12.5)	1140.4 (29.5)	1138.2 (21.6)
Ring stretching	1577.2 (22.8)	1588.2 (10.6)	1590.6 (97.7)
Common band			
Substrate + analytes	~1364-1378	1380.3 (31.6)	1382.9 (45.9)

Rs: Peak Center (cm^{-1}).

w: Full Width at Half Maximum (FWHM) (cm^{-1}).

Values obtained through Pseudo-Voigt adjust curve.

Sensor Reusability via UV Cleaning

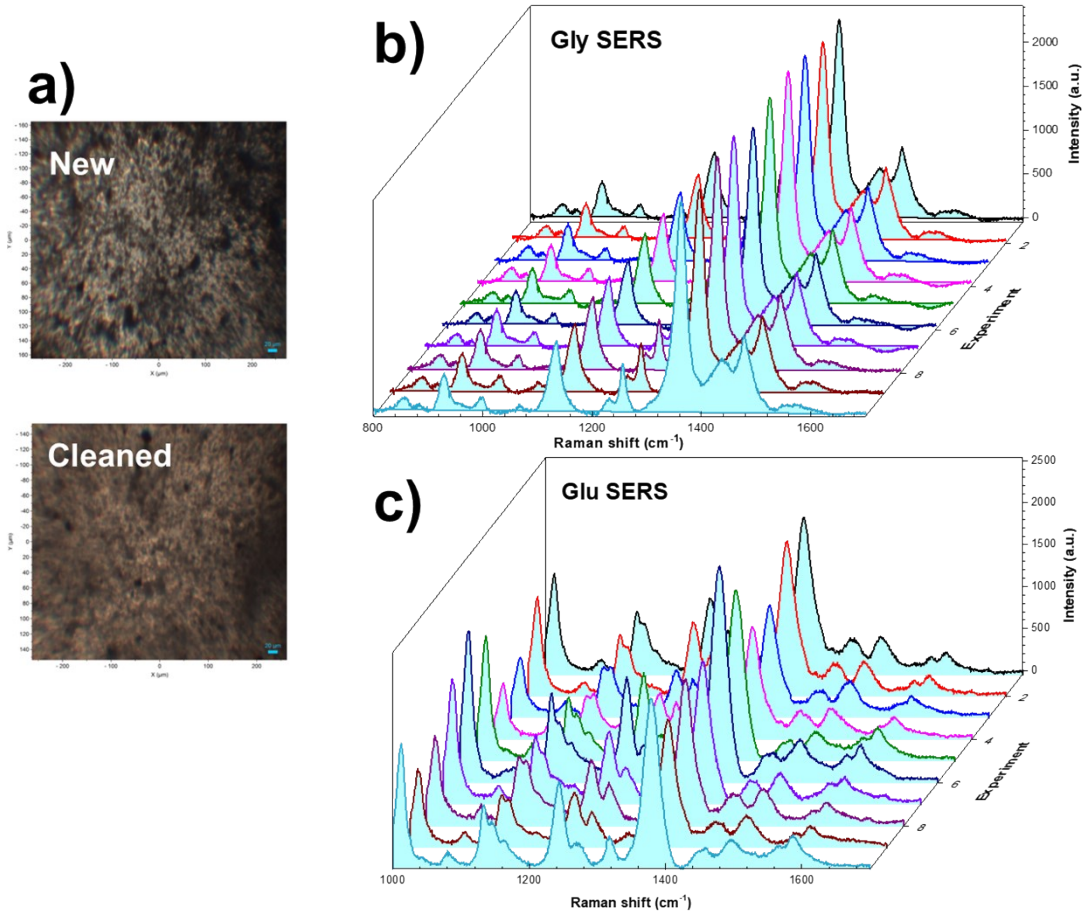

Figure S16. a) Evidence of the SERS substrate corresponding to ZnO/Au-5 before and after the UV cleaning procedure. SERS spectra of b) glyphosate, and c) glufosinate in the ZnO/Au-5 substrate after repetitive cleaning procedures.

Table S12. SERS average intensity, standard deviation, and relative standard deviation for the characteristic bands used for glyphosate detection.

Stability			
Characteristic SERS band (cm^{-1})	Average intensity (a.u.)	Standard Deviation	Relative Standard Deviation (%)
1136	716.60	34.04	4.75
1260	515.81	20.78	4.03
1370	2208.66	100.06	4.53
1480	769.32	37.07	4.81
Repeatability			
Characteristic SERS band (cm^{-1})	Average intensity (a.u.)	Standard Deviation	Relative Standard Deviation
1136	788.73	40.87	5.18
1260	533.05	24.47	4.59
1370	2279.77	142.62	6.25
1480	827.46	26.22	3.17
Reproducibility			
Characteristic SERS band (cm^{-1})	Average intensity (a.u.)	Standard Deviation	Relative Standard Deviation
1136	768.50	24.26	3.16
1260	458.13	34.49	7.53
1370	2314.13	41.1	1.77
1480	824.75	13.74	1.66

Stability: n = 30 days.

Repeatability: n = 20 measurements.

Reproducibility: n = 4 sensors

Table S13. SERS average intensity, standard deviation, and relative standard deviation for the characteristic bands used for glufosinate detection.

Stability			
Characteristic SERS band (cm^{-1})	Average intensity (a.u.)	Standard Deviation	Relative Standard Deviation (%)
1138	691.63	137.88	19.94
1370	1718.64	411.14	23.92
1441	273.78	74.27	27.13
1484	349.95	59.70	17.06
Repeatability			
Characteristic SERS band (cm^{-1})	Average intensity (a.u.)	Standard Deviation	Relative Standard Deviation (%)
1138	701.09	142.91	20.38
1370	1751.19	368.74	21.06
1441	278.99	72.80	26.10
1484	353.15	48.59	13.76
Reproducibility			
Characteristic SERS band (cm^{-1})	Average intensity (a.u.)	Standard Deviation	Relative Standard Deviation (%)
1138	701.09	97.59	13.92
1370	1751.19	162.51	9.28
1441	278.99	23.72	8.50
1484	353.15	0.54	0.15

Stability: n = 30 days.

Repeatability: n = 10 measurements.

Reproducibility: n = 4 sensors.

Analysis of real samples with glyphosate and glufosinate

Table S14. SERS quantification of glyphosate and ammonium glufosinate in soil samples at various depths and time points

Sampling day	Soil depth (cm)	Raman shift (cm^{-1})	Intensity (a.u.)	Average intensity (a.u.)	Standard deviation	Concentration (mol L^{-1})
Glyphosate						
1	0	1138	78 81 77	80.34	4.74	2.86E-22
		1370	246 232 235	237.7	7.37	2.64E-23
	20	1138	61 67 60	62.83	3.71	1.10E-22
		1370	229 252 227	235.87	13.92	1.18E-21
	50	1370	119 131 118	122.57	7.23	2.07E-22
		1138	28 31 28	28.84	1.70	1.72E-23
7	0	1370	51 56 51	52.53	3.10	7.02E-23
	20	1138	73 80 72	75.19	4.44	2.16E-22
		1370	248 272 245	255.44	15.09	1.60E-21
	50	1138	137 151 136	141.11	8.33	7.85E-21
		1370	209 230 207	215.27	12.71	8.62E-22
Glufosinate						
1	0	1370	160 176 158	164.8	9.73	3.96E-22

7	50	1370	229 252 227	235.87	13.93	1.18E-21

Table S15. SERS quantification of glyphosate in plant shoot systems and roots

Plant part	Raman shift (cm^{-1})	Intensity (a.u.)	Average intensity (a.u.)	Standard deviation	Concentration (mol L^{-1})
Glyphosate					
Root	1138	196	194.67	18.04	1.46E-19
		176			
		212			
	1370	549	545.33	49.60	1.39E-19
		494			
		593			
	1440	110	109.33	10.02	2.88E-21
		99			
		119			
Fruit	1138	104	103.33	9.02	9.99E-22
		94			
		112			
	1370	286	284.00	26.06	2.49E-21
		257			
		309			
	1440	67	66.33	6.03	1.36E-22
		60			
		72			
Stem	1138	76	75.33	7.02	2.19E-22
		68			
		82			
	1370	320	318.00	29.05	4.19E-21
		288			
		346			
	1440	78	77.33	7.02	2.97E-22
		70			
		84			
Leaves	1138	395	392.67	35.56	6.99E-15
		356			
		427			
	1370	1056	1048.67	95.21	3.26E-16
		950			
		1140			
	1440	189	187.67	17.04	7.90E-19
		170			
		204			

Table S16. SERS quantification of ammonium glufosinate in plant shoot systems and roots

Plant part	Raman shift (cm^{-1})	Intensity (a.u.)	Average intensity (a.u.)	Standard deviation	Concentration (mol L^{-1})
Ammonium glufosinate					
Root	1370	281 253 304	279.33	25.54	2.30E-21
	1440	62 56 67	61.67	5.51	9.51E-23
Fruit	1370	162 146 175	161.00	14.53	3.73E-22
	1440	57 51 62	56.67	5.51	6.67E-23

References

Albarghouthi, N., et al., 2022. Electrochemical Surface-Enhanced Raman Spectroscopy (EC-SERS) and Computational Study of Atrazine: Toward Point-of-Need Detection of Prevalent Herbicides. The Journal of Physical Chemistry C. 126**,** 9836-9842.

Bharti, K., et al., 2021. Green Synthesis of Luminescent Gold-Zinc Oxide Nanocomposites: Cell Imaging and Visible Light–Induced Dye Degradation. Frontiers in Chemistry. Volume 9 - 2021.

Cachet, N., et al., 2014. Esterification of organosolv lignin under supercritical conditions. Industrial Crops and Products. 58**,** 287-297.

Calzolari, A., Nardelli, M. B., 2013. Dielectric properties and Raman spectra of ZnO from a first principles finite-differences/finite-fields approach. Scientific reports. 3**,** 2999.

Cara, E., et al., 2020. Towards a traceable enhancement factor in surface-enhanced Raman spectroscopy. Journal of Materials Chemistry C. 8**,** 16513-16519.

Chen, Y., et al., 2022. Self-templated synthesis of mesoporous Au-ZnO nanospheres for seafood freshness detection. Sensors and Actuators B: Chemical. 360**,** 131662.

Cong, S., et al., 2020. Surface Enhanced Raman Scattering Revealed by Interfacial Charge-Transfer Transitions. The Innovation. 1.

Fodil Cherif, M., et al., 2020. Comparison of the Physicochemical Properties and Thermal Stability of Organosolv and Kraft Lignins from Hardwood and Softwood Biomass for Their Potential Valorization. Waste and Biomass Valorization. 11**,** 6541-6553.

González-Fuentes, F. J., et al., Developing a CNT-SPE Sensing Platform Based on Green Synthesized AuNPs, Using Sargassum sp. Sensors, Vol. 20, 2020.

Holanda, R. O., et al., 2020. High pressure Raman spectra and DFT calculation of glyphosate. Spectrochimica Acta Part A: Molecular and Biomolecular Spectroscopy. 242**,** 118745.

Hu, J., et al., 2022. Raman spectrum classification based on transfer learning by a convolutional neural network: Application to pesticide detection. Spectrochimica Acta Part A: Molecular and Biomolecular Spectroscopy. 265**,** 120366.

Hussin, M. H., et al., 2013. Physicochemical characterization of alkaline and ethanol organosolv lignins from oil palm (Elaeis guineensis) fronds as phenol substitutes for green material applications. Industrial Crops and Products. 49**,** 23-32.
Kamkrua, N., et al., 2023. Au Nanoparticle-Based Surface-Enhanced Raman Spectroscopy Aptasensors for Paraquat Herbicide Detection. ACS Applied Nano Materials. 6**,** 1072-1082.
López-Miranda, J. L., et al., Sargassum Influx on the Mexican Coast: A Source for Synthesizing Silver Nanoparticles with Catalytic and Antibacterial Properties. Applied Sciences, Vol. 11, 2021a.
López-Miranda, J. L., et al., 2023. Sargassum natans I algae: an alternative for a greener approach for the synthesis of ZnO nanostructures with biological and environmental applications. Marine Drugs. 21**,** 297.
López-Miranda, J. L., et al., Green Synthesis of Homogeneous Gold Nanoparticles Using Sargassum spp. Extracts and Their Enhanced Catalytic Activity for Organic Dyes. Toxics, Vol. 9, 2021b.
Makuła, P., et al., 2018. How To Correctly Determine the Band Gap Energy of Modified Semiconductor Photocatalysts Based on UV–Vis Spectra. The Journal of Physical Chemistry Letters. 9**,** 6814-6817.
Moubarik, A., et al., 2015. Understanding the physicochemical properties of olive kernel to be used as a potential tool in the development of phenol-formaldehyde wood adhesive. International Journal of Adhesion and Adhesives. 61**,** 122-126.
O'Boyle, N. M., et al., 2008. Cclib: a library for package-independent computational chemistry algorithms. Journal of computational chemistry. 29**,** 839-845.
Qiu, T., et al., 2025. SERS-based simplified analysis of paraquat in poisoning cases: Bypassing complicated pretreatment with antioxidant sensor. Spectrochimica Acta Part A: Molecular and Biomolecular Spectroscopy. 329**,** 125593.
Raji, R., Gopchandran, K. G., 2019. Plasmonic photocatalytic activity of ZnO:Au nanostructures: Tailoring the plasmon absorption and interfacial charge transfer mechanism. Journal of Hazardous Materials. 368**,** 345-357.
Schell, J. M., et al., 2015. Recent Sargassum inundation events in the Caribbean: Shipboard observations reveal dominance of a previously rare form. Oceanography. 28**,** 8-11.
Singh, S., et al., 2023. Rapid Detection of Paraquat Pesticide in Honey Using SERS-Based Portable Nanosensing Platform. IEEE Sensors Letters. 7**,** 1-4.
Song, X., et al., 2022. Specific iodide effect on surface-enhanced Raman scattering for ultra-sensitive detection of organic contaminants in water. Spectrochimica Acta Part A: Molecular and Biomolecular Spectroscopy. 272**,** 120950.
Tang, J., et al., 2019. Sensitive surface-enhanced Raman scattering detection of atrazine based on aggregation of silver nanoparticles modified carbon dots. Talanta. 201**,** 46-51.
Ye, Z., et al., 2021. Facile synthesis of ZnO doped with Au nanoparticles for sensitive and reliable photoelectrochemical detection of glucose. Ionics. 27**,** 4449-4459.
Zanasi, G., et al., Sensing Atrazine Herbicide Degradation Products through Their Interactions with Humic Substances by Surface-Enhanced Raman Scattering. Chemosensors, Vol. 9, 2021.